Effect of second-phase particle morphology on grain growth kinetics

Kunok Chang[*], Weiming Feng, Long-Qing Chen

Department of Materials Science and Engineering, The Pennsylvania State University, University Park, PA 16802, USA

Abstract

Second-phase particles are often employed to inhibit grain growth in polycrystalline metals and ceramics. In this work, we studied the effect of second-phase particle morphology on the effectiveness of inhibiting grain boundary migration using the phase-field method. We employed a multi-order parameter phase-field model in combination with an efficient memory allocation strategy which allows large-scale and coalescence-free grain growth simulations. We analyzed the dependence of pinning forces on the particle size and shape, and performed computer simulations of grain growth in the presence of second-phase particles with different sizes and varying aspect ratios. We also discuss the relationship between the pinned grain size and size distributions.
© 2009 Acta Materialia Inc. Published by Elsevier Ltd. All rights reserved.

1. Introduction

Incorporating second-phase particles is one of the most effective ways to slow or freeze grain growth of polycrystalline materials [1–3]. Second-phase particles act as obstacles to the motion of grain boundaries and thus retard grain growth. Due to their importance in the processing and application of various engineering materials, grain growth in the presence of second-phase particles has been a subject of great interest for many decades [1–5]. Our current understanding of grain growth with second-phase particles relies largely on the 60-year-old Zener theory [6,7] for predicting the effect of second-phase particles on grain growth kinetics. In his theory, Zener assumed that second-phase particles were spherical, mono-sized, and randomly distributed, and they did not coarsen. Most of these assumptions and approximations remain in all subsequent attempts [2,5] to improve upon the Zener theory. Furthermore, as in the original Zener theory, essentially all existing studies focus on the effects of the volume fraction and average size of second-phase particles on the final pinned size of the matrix grains. In reality, the morphology of second-phase particles can be rather complicated, ranging from spherical to plate-like and needle-shaped [4,8]. As pointed out by Nes et al. [5], the morphology of second-phase particles significantly affects the magnitude of pinning forces acting on a moving grain boundary. Therefore, the main objective of this work is to examine the effect of different morphologies of second-phase particles in slowing down the grain growth of matrix grains or in reducing the final pinned grain size.

We employed the phase-field method to simulate grain growth kinetics in the presence of second-phase particles. Although there have been many attempts to model the Zener pinning process using various computational approaches such as the Monte Carlo Potts model [9–11], vertex method [12] and finite element [13], the role of the morphology or size distribution of the second-phase particles has not been extensively investigated. Similar to a number of existing phase-field simulations [14–16]), we treat the second-phase particles as inert particles, i.e. they do not coarsen although modeling the grain growth in the presence of evolving second-phase particles is possible. In practice, the size of second-phase particles is not uniform, and hence we will also discuss the effect of particle size distribution.

[*] Corresponding author. Tel.: +1 814 222 5070.
  E-mail address: kuc142@psu.edu (K. Chang).

2. Simulation details

2.1. Phase-field model for grain growth with second-phase particles

Following the original grain growth model, we describe a grain structure using a set of order parameters ($\eta_1, \eta_2, \ldots, \eta_P$), each of which contains the information about the spatial distribution of grains of a given orientation. Assuming that the total number of the order parameter is P, to distinguish the two types of grains in a two-phase microstructure, we simply evolve only Q ($Q < P$) number of order parameters. These parameters represent the matrix grains while the remaining order parameters ($Q - P$) describing the inert second-phase particles remain static.

The grain boundary migration, and thus the evolution of the matrix grains, is described by the solutions to the time-dependent Ginzburg–Landau equations for each evolving order parameter,

$$\frac{\partial \eta_i}{\partial t} = -L_i \left(\frac{\delta F}{\delta \eta_i} \right), \quad i = 1, 2, \ldots, Q \tag{1}$$

where L_i are constants related to grain boundary mobility. F is the total free energy of a grain structure in terms of all order parameters and their gradients,

$$F = \int_V \left[f(\eta_1, \eta_2, \ldots, \eta_P) + \frac{1}{2} \sum_{i=1}^P \kappa_i (\nabla \eta_i)^2 \right] dV \tag{2}$$

where f is the local free energy density as a function of order parameters η_i, and κ_i are the gradient energy coefficients. The function f is constructed in such a way that it has an infinite number of degenerate minima with equal potential well depth compared to the state with all order parameters equal to zero. In practice, any finite system of a grain structure can be represented by a finite set of order parameters. We choose a free energy whose minima are located at ($\eta_1, \eta_2, \ldots, \eta_P = (1, 0, \ldots, 0), (0, 1, \ldots, 0), \ldots (0, 0, \ldots, 1)$).

We adopt the original free energy model proposed by Yang and Chen [17] for the single-phase grain growth:

$$f(\eta_1, \eta_2, \ldots, \eta_P) = \sum_{i=1}^Q \left(-\frac{1}{2} \alpha \eta_i^2 + \frac{1}{4} \beta \eta_i^4 \right) + \gamma \sum_{i=1}^P \sum_{j \neq i}^Q \eta_i^2 \eta_j^2 \tag{3}$$

where α, β and γ are phenomenological parameters. The free energy has $2P$ minima representing $2P$ different orientations of the grains since one order parameter has two equivalent values ($\eta_i = \pm 1$). Plugging Eqs. (2) and (3) into the evolution Eq. (1), we have

$$\frac{\partial \eta_i}{\partial t} = -L_i \left(-\alpha \eta_i + \beta \eta_i^3 + 2\gamma \eta_i \sum_{j \neq i}^P \eta_j^2 - \kappa_i \nabla^2 \eta_i \right), \quad i = 1, 2, \ldots, Q \tag{4}$$

or

$$\frac{\partial \eta_i}{\partial (L_i t)} = \eta_i \left(\alpha - (\beta - 2\gamma) \eta_i^2 - 2\gamma \sum_{j=1}^P \eta_j^2 \right) + \kappa_i \nabla^2 \eta_i, \quad i = 1, 2, \ldots, Q \tag{5}$$

2.2. Numerical algorithms

Numerical solutions of the kinetic Eqs. (4) and (5) yield the order parameter fields as a function of time and thus the temporal grain structure evolution. One of the drawbacks in the original implementation [17] of the grain growth model is the difficulty in avoiding the coalescence of grains during grain growth. Although using a large number of order parameters will decrease the frequency of coalescence, it is at the expense of increasing the computational time. Krill and Chen [18] made the first attempt to reduce or eliminate the coalescence while keeping the number of order parameters small by proposing a dynamic order parameter reassignment algorithm. More recently, a number of more efficient approaches have been proposed for coalescence-free grain growth simulations using the multi-order parameter phase-field model. For example, Vedantam and Patnaik [19] developed an active parameter tracking (ATP) method to reduce not only computational time but also memory while keeping the number of equations to be solved at a given time and location small. A similar idea was proposed by Gruber et al. based on the sparse data structure [20] and by Vanherpe et al. using the so-called "bounding box algorithm" [21]. A similar strategy of active parameter tracking was also implemented in the multiphase model of grain growth [22]. In this work, we followed the active parameter tracking algorithm proposed by Vedantam and Patnaik [19]. In this approach, the number of active order parameters at each simulation grip point remains small (usually less than 10) even when a large number of order parameters are employed for the model. The evolution equations are only solved for the active order parameters near grain boundaries. Since the number of grain boundaries decreases as the overall size of the grains grow, the simulation becomes increasingly more efficient as a function of time. With a sufficient number of order parameters, e.g., when the number of order parameters is equal to the number of grains in the initial microstructure, complete coalescence-free simulations can be carried out.

In order to implement the active parameter tracking algorithm, instead of employing the more efficient and accurate semi-implicit Fourier spectral method [23], we applied the simple forward-Euler scheme to descretize the time derivatives:

$$\eta_i(t + \Delta t) = \eta_i(t) + \frac{d\eta_i}{dt} \Delta t \tag{6}$$

2.3. Simulation conditions

To investigate the effect of size distributions and morphology of second-phase particles on the grain growth kinetics, we used a model system rather than a specific material. The values of the parameters used in this study are given in non-dimensional units. We performed two-dimensional simulations with a system size of 2048×2048 grid points and a

grid size $dx = 1$. We chose $\alpha_i = \beta_i = \gamma_i = 1$ for the coefficients in the free energy function. The gradient coefficient $\kappa_i = 2.0$, and the kinetic constant $L_i = 1$ for all order parameters. We chose the time step (dt) as 0.1. We employed a total of 32,000 order parameters. We applied periodic boundary conditions to all simulations. Performing simulations with 2048×2048 grid points and 32,000 order parameters for 30,000 time steps takes approximately 13 h and a maximum of 1.85 GB memory on an average PC.

3. Results

3.1. Effect of second-phase size distribution

In general, the size of second-phase particles in a system is not uniform. We first examine the influence of particle size distributions on the grain growth kinetics. The system size is 2048×2048 grid points with 32,000 order parameters which represent the grain orientation of every individual grain. The area fraction of the circular second-phase particles is 7%, and all particles are randomly distributed. The fraction of the second-phase particles in the simulations is given by fraction $= \frac{\text{Number of grids indicating second phase} \times 100}{\text{Total grid points of the system } (2048^2)}$ (%). In the mono-sized particle case, the number of the particles is given as $\frac{\text{area of total second phase}}{\text{area per one particle}}$. We consider three types of distributions – the mono-sized particles, the uniform size distribution and the normal size distribution. The average area of the second-phase particle is 197 for all three cases and the area fraction of the second-phase particles is 7% for all cases. The number of particle centers is given as 1484 for all cases. The distributions of the particle areas are shown in Fig. 1a and b for the uniform and normal distributions. In reality, we can describe all particle size distributions as normal distributions. If the standard deviation is infinite, it corresponds a uniform distribution. On the other hand, the standard deviation of the second-phase particle size distribution should be zero in the mono-sized case. As shown in Fig. 2, the effect of the particle size distribution is not notable during single-phase grain growth with inert second-phase particles. The pinned diameter in the presence of mono-sized, uniformly distributed, and normally distributed second-phase particles are approximately the same as long as the number of particles and volume fractions are the same. We performed at least three simulations for each case and these repetitions gave consistent results.

3.2. Effect of second-phase particle size

It was shown above that the pinned grain size is rather independent of particle size distribution as long as the volume fraction, the average size, and the number of second-phase particles remain the same for the different distributions. In this section, we discuss the effect of particle size. In our simulations, second-phase particles of uniform size were randomly distributed, and all particles were separated from each other at least 12 grids apart. We fixed the
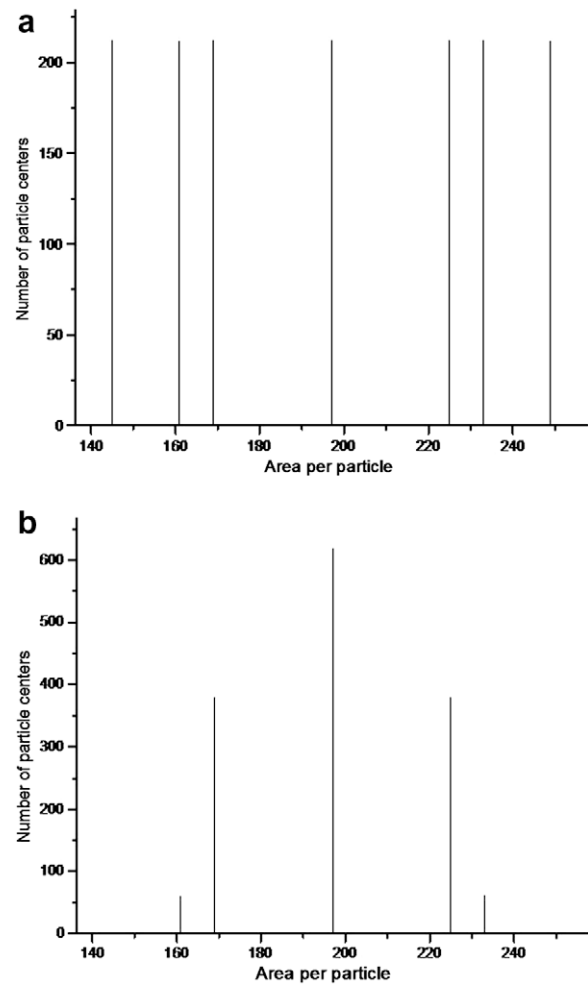

Fig. 1. (a) The uniform size distribution of the second-phase particle area placed on the matrix. (b) The normal size distribution of the second-phase particle area placed on the matrix.
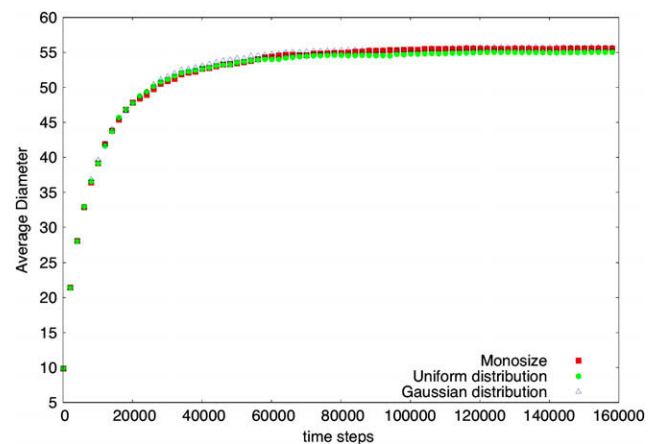

Fig. 2. Average grain size evolution for the mono-size particle case, the normal distribution case and the uniform distribution case. The system size is 2048×2048 and initially 32,000 grains are randomly distributed. The fraction of the second-phase is 7% and the number of particle centers is 1490 for all cases.

volume fraction for second-phase mono-sized particles at 7%. The system size is 2048 × 2048, and 32,000 grains are initially distributed. Examples of grain structures without second-phase particles and with 7% second-phase particles are shown in Fig. 3a and b. At 70,000 time steps, the number of grains in the microstructure without particles was 262. With the 7% second-phase particles, the number of grains was 706. In the 7% particle case, most of the second-phase particles were at the grain boundaries. This results indicate that, in two-dimensional grain growth with inert second-phase particles, almost all inert particles are effective in pinning grain boundary movement.

The average grain diameter is plotted as a function of time for several different sizes of second-phase particles in Fig. 4. The grain size reached a stationary state for all particle sizes. Furthermore, the limiting grain size decreased as the second-phase particle size decreased, i.e. small second-phase particles are more efficient than large particles, given the same volume fraction and morphology. Fig. 4 shows the limiting diameter as a function of second-phase particle size. These results are consistent with Zener's prediction [1], which shows a linear relationship between the pinned grain diameter and a homogenous particle radius.

The presence of second-phase particles also affects the grain size distribution. For example, the peak of the grain size distribution shifts to smaller values as a function of time (Fig. 5). For the pinned grain structure, the peak value of the grain size distribution is smaller than the average grain diameter. This result means that second-phase particles prevent the elimination of small grains.

3.3. Effect of second-phase particle aspect ratio

We thus far look at the effect of second-phase particle average size and size distributions on pinned grain growth. We will now consider one of the less-studied morphological factors in this system, the effect of second-phase aspect ratio. The original Zener relation assumed a spherical shape for all second-phase particles. We plot the average grain size as a function of time for several different aspect ratios of second-phase particles in Fig. 6. From this plot, we can see that the pinning effect increases when the aspect ratio ($\varepsilon = \frac{b}{a}$, where a, b indicate two axes) of the particle is deviated from 1. An aspect ratio much larger or smaller than 1 indicates needle-shaped particles, while an aspect ratio of 1 denotes circular particles in the two-dimensional space. Therefore, simply speaking, needle-shaped particles are more effective in terms of pinning, as compared to circular particles of the same size. There are more grains in a pinned grain structure with high aspect ratio second-phase particles than in a grain structure with more isotropic particles. In our simulations, the number of grains was 706 for an aspect ratio 1.00 and 948 for an aspect ratio of 8.91 (0.11). This result is consistent with our average particle size calculation.

We also examined the role of the alignment directions of the needle-shaped particles. In particular, we considered
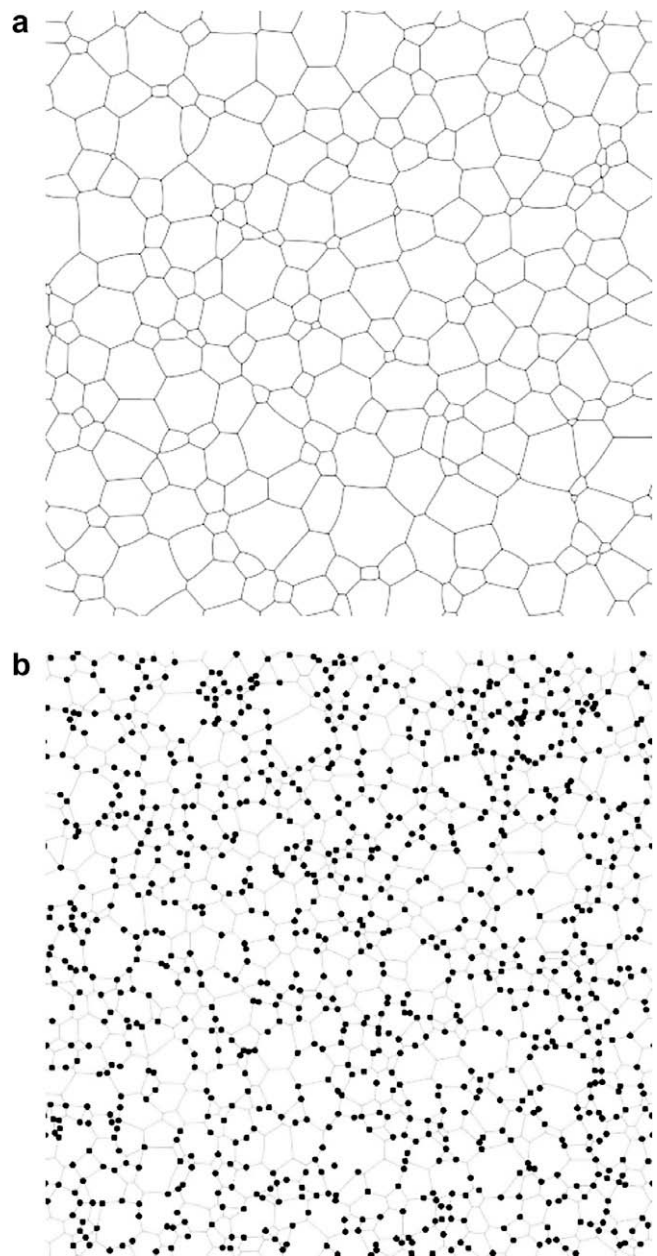

Fig. 3. (a) Morphology pattern at 70,000 time steps with no second-phase particles. The system size is 2048 × 2048 and, initially, 32,000 grains are randomly distributed. (b) Morphology pattern at 70,000 time steps with 7% second-phase particles. The system size is 2048 × 2048 and, initially, 32,000 grains are randomly distributed.

the case in which all of the particles are aligned along the same direction and another case with the second-phase particles are distributed between two directions oriented at 90° from each other (Fig. 7). In the two-direction case, an equal number of particles were oriented along each direction. The system size was 2048 × 2048, and second-phase particle fraction was 7% in both cases. The area per particle was 317 grid points. The half length of the long axis was 29.4, and the half length of the short axis was 3.3. According to Fig. 8, the case with all second-phase particles aligned along one direction was slightly more efficient at pinning
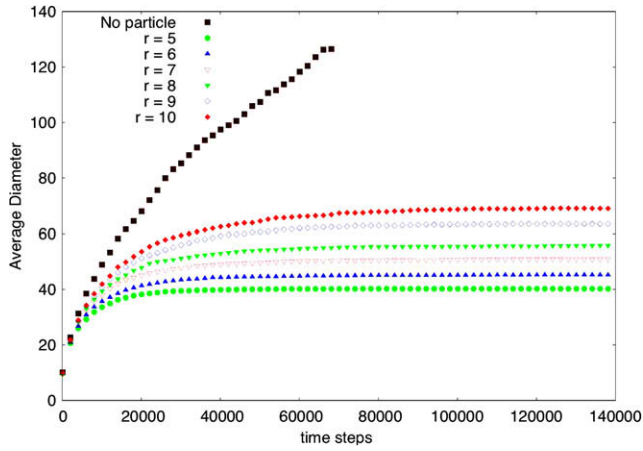
Fig. 4. Time evolution of the average grain diameter with the mono-sized, spherical, randomly distributed particles. The system size is 2048 × 2048 grid points with 32,000 order parameters.

Fig. 6. Average grain radius versus time for different particle aspect ratios. For all cases, the area fraction of the second-phase particles was 7%, and is the particles were randomly distributed, mono-sized, and aligned along one direction. The system size is 2048 × 2048 grid points with 32,000 order parameters.

$$F_{total} = \int_0^{\pi/2} F \, d\theta = \int_0^{\pi/2} 2\sigma_{gb} \sin\theta \, d\theta = 2\sigma_{gb} \qquad (8)$$

According to the sharp grain boundary model, the maximum and the total dragging force show no particle size dependence. Only the number of particle centers and the grain boundary energy determine the dragging force in a two-dimensional system. Thus, it is not surprising that the particle size distribution plays no role in determining the overall pinning effect, and it was confirmed in Fig. 2.

To better understand observations and results of our simulations, we designed a simple system shown in Fig. 10. Assuming that the driving force to move a grain boundary is constant, we derived the relation between a driving force (Δf) and a velocity of a straight grain boundary without a second-phase particle as follows:

$$v = \left(\frac{L\kappa}{\sigma_{gb}}\right)\Delta f \qquad (9)$$

where σ_{gb} is the grain boundary energy given by

$$\sigma_{gb} = \int_0^\infty \left[f(\eta_1, \eta_2) - f(\eta_1^{eq}, \eta_2^{eq}) + \frac{\kappa}{2}\left(\left(\frac{\partial\eta_1}{\partial x}\right)^2 + \left(\frac{\partial\eta_2}{\partial x}\right)^2 \right) dx \right] \qquad (10)$$

L is the mobility and κ is the gradient coefficient.

Consequently, Eq. (3) is modified as follows:

$$f(\eta_1, \eta_2) = \sum_{i=1}^2 \left(-\frac{1}{2}\alpha\eta_i^2 + \frac{1}{4}\beta\eta_i^4 \right) + \gamma \sum_{i=1}^2 \sum_{j\neq i}^2 \eta_i^2\eta_j^2 + \Delta f\eta_1 \qquad (3')$$

Plugging Eq. (3') into Eq. (1) we have

$$\frac{\partial\eta_1}{\partial t} = -L_1(-\alpha\eta_1 + \beta\eta_1^3 + 2\gamma\eta_1\eta_2^2 - \kappa_1\nabla^2\eta_1 + \Delta f) \qquad (4')$$

than the two-direction case. Since a large number of small grains were captured by two parallel needle-shaped particles, the unidirectional aligned case showed a more efficient pinning effect.

4. Discussion

4.1. Dragging force applied by a single second-phase particle

According to previous research [7,24], a single second-phase particle applies the pinning force only at two singular points (A and B in Fig. 9). The magnitude of the dragging force along the x direction is given as follows:

$$F = 2\sigma_{gb}\sin\theta \qquad (7)$$

Thus the maximum dragging force occurs when $\theta = \frac{\pi}{2}$ and $F_{max} = 2\sigma_{gb}$. The total dragging force is derived as follows:
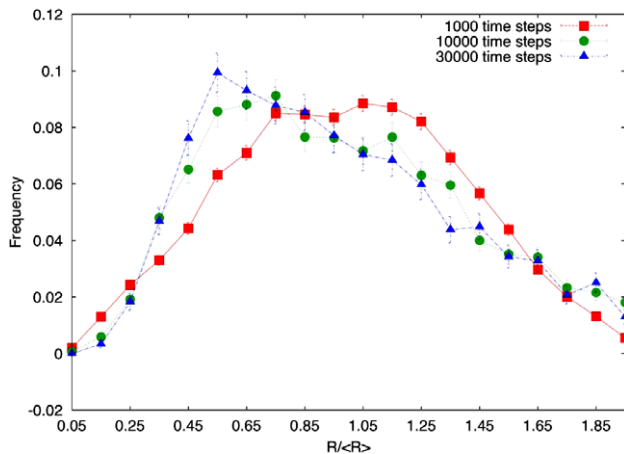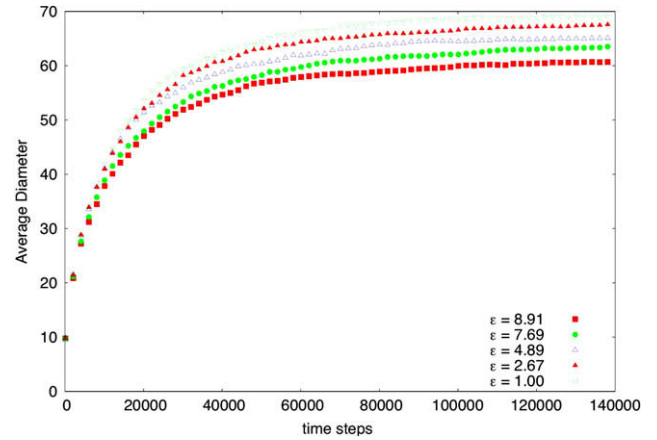

Fig. 5. Grain diameter distribution generated by a phase-field simulation. The system size is 2048 × 2048 with 32,000 order parameters. Second-phase spherical, mono-sized particles ($r = 5$) corresponding to 7% of the total area are randomly distributed. Distributions are plotted for three time steps.
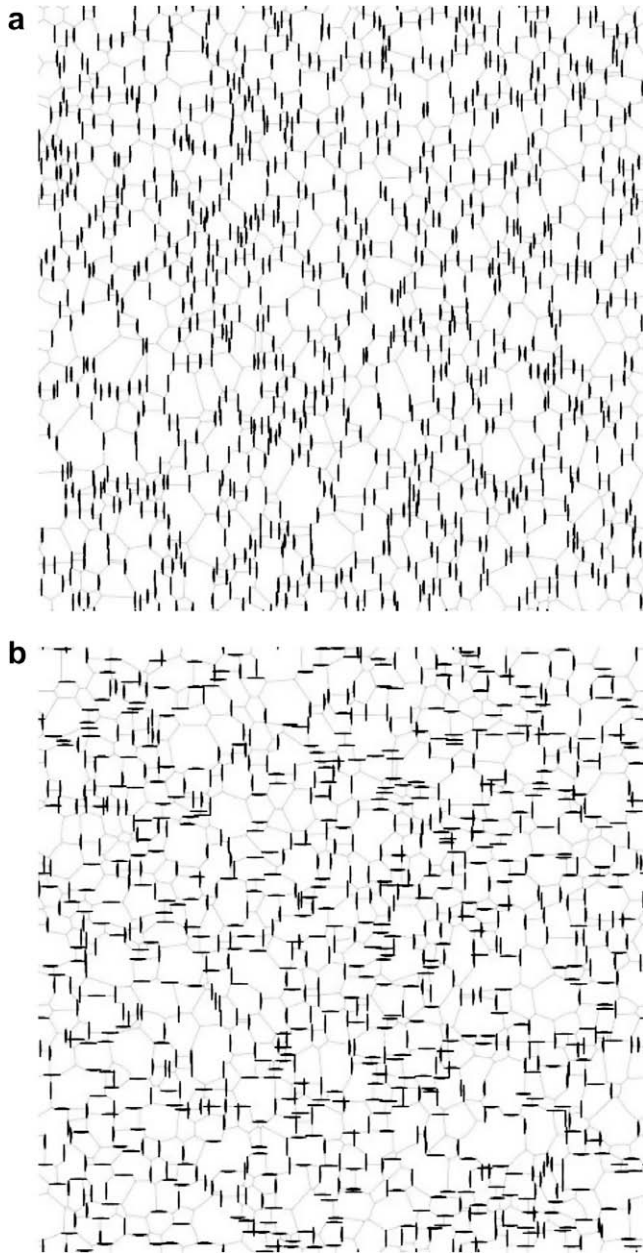
a

b

Fig. 7. (a) All second-phase particles are aligned along one direction. The system size is 2048 × 2048 with 32,000 order parameters. It takes 70,000 time steps to obtain the described microstructure. (b) All second-phase particles are aligned along two directions (right). The system size is 2048 × 2048 with 32,000 order parameters. It takes 70,000 time steps to obtain the described microstructure.

$$\frac{\partial \eta_2}{\partial t} = -L_2(-\alpha\eta_2 + \beta\eta_2^3 + 2\gamma\eta_2\eta_1^2 - \kappa_2\nabla^2\eta_2) \qquad (4'')$$

$$\frac{\partial \eta_1}{\partial (L_1 t)} = \eta_1(\alpha - (\beta - 2\gamma)\eta_1^2 - 2\gamma\eta_2^2) + \kappa_1\nabla^2\eta_1 + \Delta f \qquad (5')$$

$$\frac{\partial \eta_2}{\partial (L_2 t)} = \eta_2(\alpha - (\beta - 2\gamma)\eta_2^2 - 2\gamma\eta_1^2) + \kappa_2\nabla^2\eta_2 \qquad (5'')$$

When dragging force Δf_{drag} is applied on the grain boundary, the velocity of the contact point A in Fig. 9 function of position y ($v_{c.p.}(y)$) is given as follows:
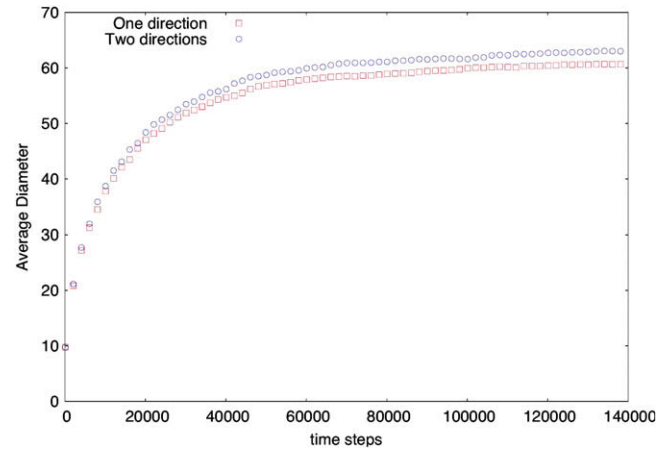

Fig. 8. Second-phase particles corresponding to 7% of the total area are placed on the 2048 × 2048 system. All particles are randomly distributed with an aspect ratio of 8.91. In the single orientation case, all particles are aligned along one direction. In the two-direction case, half of the particles are aligned along one direction and the remaining particles are aligned along the other direction, which is 90° from the first direction.
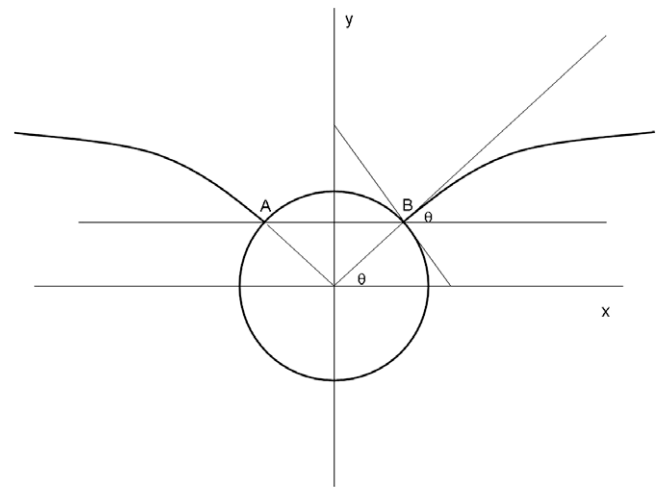

Fig. 9. Dragging of the grain boundary migration by a circular second-phase particle in the two-dimensional system.
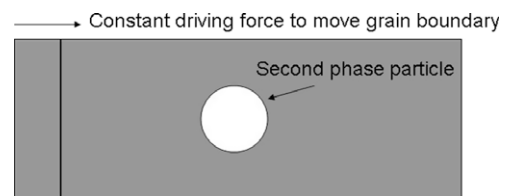

Fig. 10. Schematic drawing of the flat grain boundary moving with a single second-phase particle.

$$v_{c.p.}(y) = \left(\frac{L\kappa}{\sigma_{gb}}\right)(\Delta f - \Delta f_{drag}(y)) \qquad (9')$$

Thus, the contact point velocity decreases as the dragging force increases.

We estimated the velocity of contact point A between the particle and the grain boundary in Fig. 9 to evaluate

the dragging force. We plotted the velocity of contact point A function of position y in Fig. 11. The particle center was located at $y = 85$ and the total system size was 1500×600 and driving force Δf was chosen as 0.002. As we expected, the velocity of contact point decreased along the grain-boundary-moving direction from the particle center. The minimum velocity of contact point A in Fig. 11 is approximately constant. It is one of the evidences that the maximum dragging force does not depend on the particle size in a two-dimensional system.

4.2. Dragging force applied by two parallel particles

As discussed in Section 4.1, the maximum dragging force shows no size dependence in the case of a single second-phase particle. However, the case of many particles can be different. For example, if two second-phase particles are located close each other, then the grain boundary can be captured when $\theta \ll \frac{\pi}{2}$. In order to explain why a needle-shaped particle pins grains more effectively than a circular-shaped particle of the same size, we considered the case of a grain boundary dragged by two second-phase particles, as shown in Fig. 12b.

The equation of the ellipse in Fig. 12a is $\frac{x^2}{a^2} + \frac{y^2}{b^2} = 1$ and it is easy to derive the relation between θ and θ'.

$$\tan \theta' = \varepsilon^2 \tan \theta \left(\text{when } \varepsilon = \frac{a}{b} \right) \qquad (11)$$

In Fig. 12b, the forces applied on point A are a curvature-driven driving force and a pinning force applied by the second-phase particle. The curvature, $1/R$, of the grain boundary in Fig. 12b is given as follows:

$$\frac{1}{R} = \frac{2 \sin \theta'}{d - 2r \cos \theta} \qquad (12)$$

$$F_A = \frac{\sigma_{gb}}{R} - \sigma_{gb} \sin \theta' = \sigma_{gb} \sin \theta' \left(\frac{2}{d - 2r \cos \theta} - 1 \right) \qquad (13)$$

When $d \gg r$, we assumed that $d - 2r \cos \theta = d(1 - 2 \cos \theta \frac{r}{d}) \approx d$. Thus, Eq. (4'') can be rewritten as
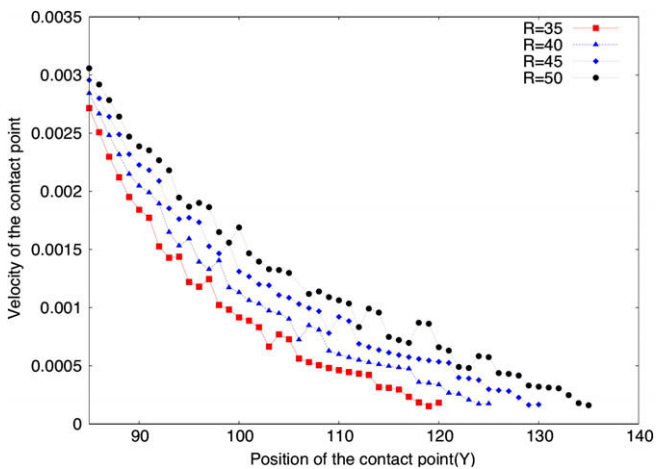

Fig. 11. Plot of the minimum velocity of the contact point A function of the position (Y).
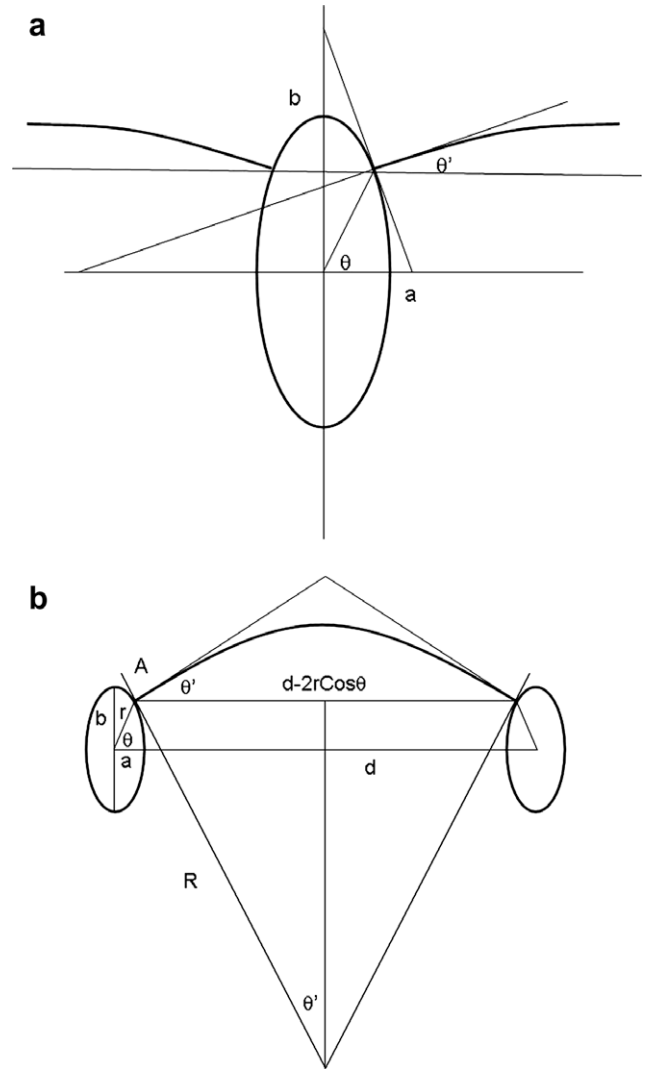

Fig. 12. (a) Dragging of the grain boundary migration by an elliptical second-phase particle in the two-dimensional system. (b) Dragging of the grain boundary migration by two elliptical second-phase particles in the two-dimensional system.
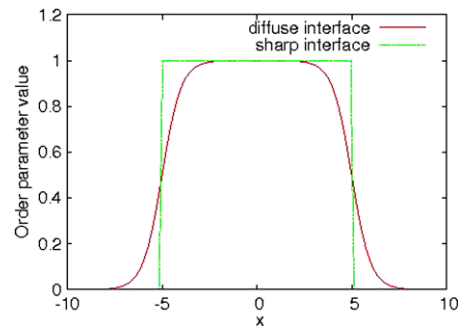

Fig. 13. The order parameter values for sharp and diffuse interfaces between second-phase particles and the matrix grains.

$F_A \approx \sigma_{gb} \sin \theta' \left(\frac{2-d}{d} \right)$. From Eq. (11), we can obtain the relation that $\sin \theta' \approx \varepsilon^2 \sin \theta$ when $\theta \ll \frac{\pi}{2}$. Finally, we have

$$F_A \approx \frac{\sigma_{gb} \varepsilon^2 \sin \theta (2 - d)}{d} \quad \left(\text{when } \theta \ll \frac{\pi}{2} \text{ and } d \gg r \right) \qquad (14)$$
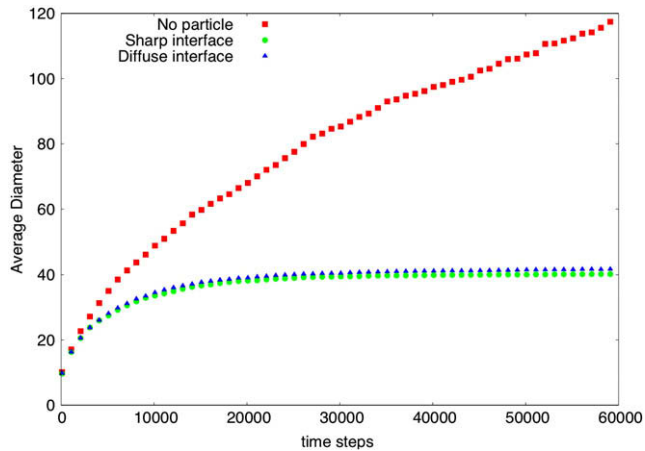
Fig. 14. Average diameter of grains as a function of time for of a sharp or diffuse interface between the matrix grains and the second-phase particles. Both results are calculated using a phase-field method. According to our simulation, the difference between these two cases is not significant.

Consequently, the driving force for moving a grain boundary at the middle of the particle decreases as the aspect ratio ε decreases. As shown in Fig. 7, many straight grain boundaries can be captured by two needle-shaped particles. This phenomenon is the main reason why needle-shaped particles are more efficient in terms of pinning force. The probability that two parallel particles are located close enough to capture a grain boundary is two times larger in the unidirectional aligned case than the two-direction case. Thus, the one direction case shows more efficient pinning, as illustrated in Fig. 8.

4.3. Interface between a particle and matrix

Finally, in the above simulations, we assumed that the interface between second-phase particles and the matrix grains are sharp, i.e. of only one grid point in thickness. To validate this assumption, we examined the effect of the diffuseness of the interface on the pinning effect. The sharp interface is described by $0.5 \times \tanh(-r + R) + 0.5$, where r and R indicate the distance from the particle center $(r = \sqrt{(x - x_p)^2 + (y - y_p)^2})$ where x_p, y_p are the positions of the particle center and the particle radius, respectively. The order parameter profile in the diffuse interface and sharp interface are shown in Fig. 13. According to Fig. 14, the interface between a particle and matrix does not play a significant role in determining the kinetics of grain growth. If there is no anisotropy in interfacial energy between a particle and the matrix, the pinning force is not affected by the interfacial energy.

5. Conclusions

We studied the effect of the average size and size distributions and morphology of second-phase particles on grain growth kinetics in two dimensions. We showed that for the same second-phase volume fraction, smaller particle sizes are more effective at pinning grain boundary motion. In contrast, the size distribution of the second-phase particles does not play a significant role in pinning. We also showed that needle-shaped second-phase particles are more effective for retarding grain growth, while the directional orientation of these needle-shaped second-phase particles has a very small effect on pinning. We are currently conducting more realistic three-dimensional simulations in which needle- and plate-shaped particles can be distinguished.

Acknowledgments

References

[1] Smith C. Trans Am Inst Min Metall Eng 1948;175.
[2] Hellman P, Hillert M. Scand J Metall 1975;4:211–9.
[3] Hillert M. Acta Metall 1988;36:3177–81.
[4] Song H, Coble RL. J Am Ceram Soc 1990;73:2086–90.
[5] Nes E, Ryum N, Hunderi O. Acta Metall 1985;33:11–22.
[6] Humphreys FJ, Ardakani MG. Acta Mater 1996;44:2717–27.
[7] Doherty R, Srolovitz D, Rollett A, Anderson M. Scripta Metall 1987;21:675–9.
[8] O'Bryan HM, Thomson J. J Am Ceram Soc 1983;66:66–8.
[9] Gao J, Thompson RG, Patterson BR. Acta Mater 1997;45:3653–8.
[10] Anderson M, Grest G, Doherty R, Li K, Srolovitz D. Scripta Metall 1989;23:753–8.
[11] Soucail M, Messina R, Cosnuau A, Kubin LP. Materials Science and Engineering A 1999;A271:1–7.
[12] Weygand D, Bréchet Y, Lépinoux J. Acta Mater 1999;47:961–70.
[13] Kim B, Kishi T. Acta Mater 1999;47:2293–301.
[14] Moelans N, Blanpain B, Wollants P. Acta Mater 2005;53:1771–81.
[15] Moelans N, Blanpain B, Wollants P. Acta Mater 2006;54:1175–84.
[16] Suwa Y, Saito Y, Onodera H. Scripta Mater 2006;55:407–10.
[17] Chen L, Yang W. Phys Rev B 1994;50:15752.
[18] Krill III CE, Chen L. Acta Mater 2002;50:3059–75.
[19] Vedantam S, Patnaik BSV. Phys Rev E 2006;73:016703–.
[20] Gruber J, Ma N, Wang Y, Rollett AD, Rohrer GS. Model Simul Mater Sci Eng 2006;14:1189–95.
[21] Vanherpe L, Moelans N, Blanpain B, Vandewalle S. Phys Rev E 2007;76:056702–11.
[22] Kim SG, Kim DI, Kim WT, Park YB. Phys Rev E 2006;74:061605–14.
[23] Fan D, Chen SP, Chen L, Voorhees PW. Acta Mater 2002;50:1895–907.
[24] Moelans N, Blanpain B, Wollants P. Acta Mater 2007;55:2173–82.